

OPEN

# High mobility approaching the intrinsic limit in Ta-doped SnO<sub>2</sub> films epitaxially grown on TiO<sub>2</sub> (001) substrates

Michitaka Fukumoto<sup>1</sup>, Shoichiro Nakao<sup>1,2</sup>✉, Kei Shigematsu<sup>2,3</sup>, Daisuke Ogawa<sup>4</sup>, Kazuo Morikawa<sup>4</sup>, Yasushi Hirose<sup>1,2</sup> & Tetsuya Hasegawa<sup>1,2</sup>

Achieving high mobility in SnO<sub>2</sub>, which is a typical wide gap oxide semiconductor, has been pursued extensively for device applications such as field effect transistors, gas sensors, and transparent electrodes. In this study, we investigated the transport properties of lightly Ta-doped SnO<sub>2</sub> (Sn<sub>1-x</sub>Ta<sub>x</sub>O<sub>2</sub>, TTO) thin films epitaxially grown on TiO<sub>2</sub> (001) substrates by pulsed laser deposition. The carrier density ( $n_e$ ) of the TTO films was systematically controlled by  $x$ . Optimized TTO ( $x = 3 \times 10^{-3}$ ) films with  $n_e \sim 1 \times 10^{20} \text{ cm}^{-3}$  exhibited a very high Hall mobility ( $\mu_H$ ) of  $130 \text{ cm}^2 \text{ V}^{-1} \text{ s}^{-1}$  at room temperature, which is the highest among SnO<sub>2</sub> films thus far reported. The  $\mu_H$  value coincided well with the intrinsic limit of  $\mu_H$  calculated on the assumption that only phonon and ionized impurities contribute to the carrier scattering. The suppressed grain-boundary scattering might be explained by the reduced density of the {101} crystallographic shear planes.

Tin dioxide (SnO<sub>2</sub>) has been extensively studied as a practical transparent oxide semiconductor in various applications such as field-effect transistors<sup>1,2</sup>, gas sensors<sup>3-5</sup>, and transparent electrodes<sup>6-8</sup>. Hall mobility ( $\mu_H$ ) is a key parameter in determining the performance of such devices, and the  $\mu_H$  values of bulk SnO<sub>2</sub> single crystals are in the range of 70 to 260  $\text{cm}^2 \text{ V}^{-1} \text{ s}^{-1}$  at room temperature<sup>9-11</sup>. However, SnO<sub>2</sub> thin films show a rather low  $\mu_H$  of less than 100  $\text{cm}^2 \text{ V}^{-1} \text{ s}^{-1}$  even in well-optimized epitaxial films<sup>12,13</sup>, which limits the practical use of SnO<sub>2</sub>.

The lower  $\mu_H$  in SnO<sub>2</sub> epitaxial thin films is primarily attributable to the lack of lattice-matched substrates. Thus far, corundum Al<sub>2</sub>O<sub>3</sub> and rutile TiO<sub>2</sub> have been widely used as the substrates for the epitaxial growth<sup>14,15</sup> of SnO<sub>2</sub>. Particularly, Al<sub>2</sub>O<sub>3</sub>, with a high thermal and chemical stability, is suitable for the growth of SnO<sub>2</sub> thin films at high temperatures, but the SnO<sub>2</sub> thin films deposited on Al<sub>2</sub>O<sub>3</sub> suffer from lowered crystallinity owing to the difference between the crystal structures of the film and substrate. For example, very low  $\mu_H$  values are frequently observed for epitaxial SnO<sub>2</sub> films on Al<sub>2</sub>O<sub>3</sub>. TiO<sub>2</sub> shares the same rutile structure as SnO<sub>2</sub>, but it has a relatively large lattice-mismatch with SnO<sub>2</sub>, which is 3.1% and 7.7% for the  $a$ -axis and  $c$ -axis, respectively. Indeed, it was reported that  $\mu_H$  of the undoped SnO<sub>2</sub> film with (001) orientation on TiO<sub>2</sub> (001) was limited to a rather small value<sup>16</sup>, that is,  $\sim 40 \text{ cm}^2 \text{ V}^{-1} \text{ s}^{-1}$ . To overcome the above-mentioned difficulty, very thick self-buffer layers<sup>12,13</sup> have been employed to grow high- $\mu_H$  epitaxial SnO<sub>2</sub> films on Al<sub>2</sub>O<sub>3</sub>.

Another important factor for achieving high  $\mu_H$  is to control the carrier density ( $n_e$ ) because carriers play two competing roles in  $\mu_H$ ; an increase in  $n_e$  enhances the screening of the Coulomb scattering potential and thus increases  $\mu_H$ , whereas an increased amount of dopants suppresses  $\mu_H$  owing to impurity scattering. To date, much effort has been made to grow undoped<sup>13-18</sup> or heavily doped<sup>19-22</sup> SnO<sub>2</sub> films on a wide variety of substrates. Heavily doped SnO<sub>2</sub> films, albeit practically important, show a low  $\mu_H$  that is dominated by impurity scattering. Attempts to pursue high  $\mu_H$  in undoped SnO<sub>2</sub> thin films have been unsuccessful owing to the significant carrier scattering by the grain boundary<sup>18,23</sup> and dislocation<sup>13,24</sup> induced by lattice-mismatched substrates. There is a

<sup>1</sup>Department of Chemistry, The University of Tokyo, 7-3-1 Hongo, Bunkyo-ku, Tokyo, 113-8654, Japan. <sup>2</sup>Kanagawa Institute of Industrial Science and Technology (KISTEC), 705-1 Shimoimaizumi, Ebina, Kanagawa, 243-0435, Japan.

<sup>3</sup>Laboratory for Materials and Structures, Tokyo Institute of Technology, 4259 Nagatsuta, Midori-ku, Yokohama, 226-8503, Japan. <sup>4</sup>Tokyo Metropolitan Industrial Technology Research Institute (TIRI), 2-4-10 Aomi, Koto-ku, Tokyo, 135-0064, Japan. ✉e-mail: [nakao@chem.s.u-tokyo.ac.jp](mailto:nakao@chem.s.u-tokyo.ac.jp)

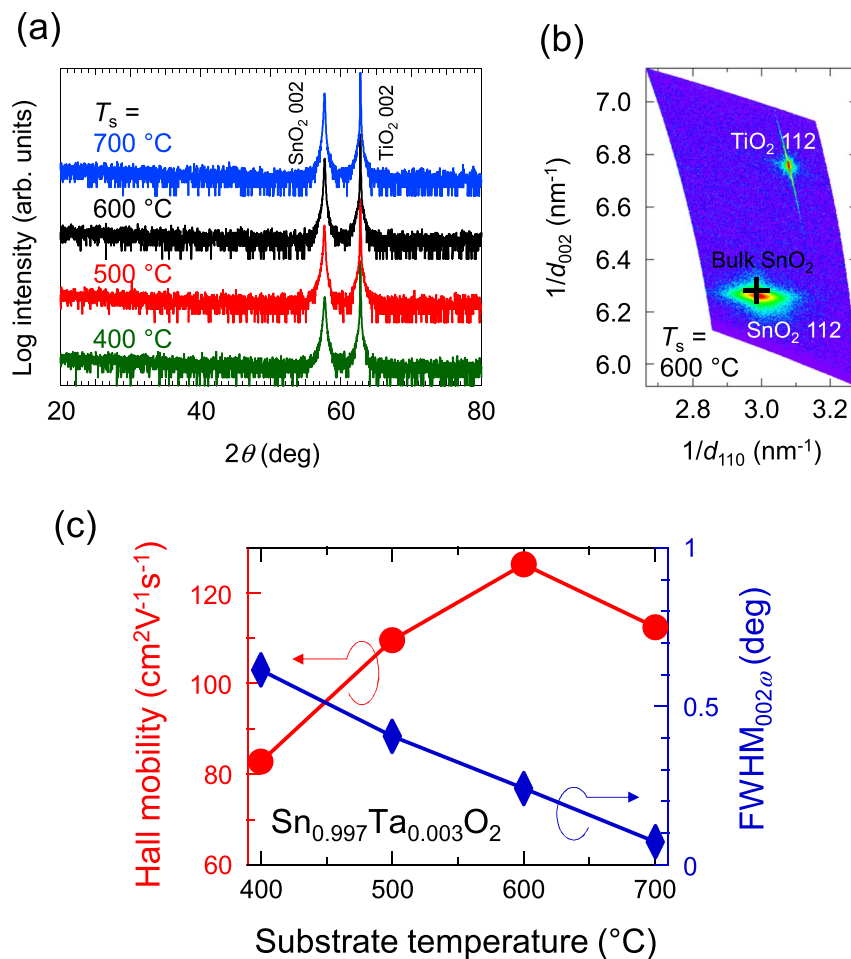


**Figure 1.** (a)  $\omega$ - $2\theta$  X-ray diffraction patterns for Sn<sub>1-x</sub>Ta<sub>x</sub>O<sub>2</sub> (TTO) films with  $x = 3 \times 10^{-3}$  grown at various substrate temperatures ( $T_s$ ). (b) A reciprocal space map around the asymmetric 112 diffraction peaks for a TTO film grown at  $T_s = 600^\circ\text{C}$ . A cross represents the peak position for bulk SnO<sub>2</sub>. (c)  $T_s$  dependence of Hall mobility ( $\mu_H$ , circles) and full width at half maximum of rocking curve ( $\omega$  scan) for 002 diffraction peak (FWHM<sub>002 $\omega$</sub> , diamonds) for the TTO ( $x = 3 \times 10^{-3}$ ) films.

possibility to realize a high mobility in the intermediate  $n_e$  region between undoped and heavily doped SnO<sub>2</sub>, but little attention has been paid to lightly doped<sup>12,23</sup> SnO<sub>2</sub> films.

In this study, we focus on lightly doped SnO<sub>2</sub> thin films to achieve a high  $\mu_H$ . We investigated the electrical transport properties of lightly Ta-doped SnO<sub>2</sub> (Sn<sub>1-x</sub>Ta<sub>x</sub>O<sub>2</sub>, TTO) films grown on TiO<sub>2</sub> (001) substrates, which are isostructural to SnO<sub>2</sub>, with the smallest lattice mismatch. We found that the increase in  $n_e$  by Ta-doping dramatically enhanced  $\mu_H$ , probably owing to a screening of the carrier scattering by the grain boundaries and dislocations. The TTO films with  $n_e \sim 1 \times 10^{20} \text{ cm}^{-3}$  exhibited  $\mu_H$  of  $130 \text{ cm}^2 \text{ V}^{-1} \text{ s}^{-1}$ , which is the highest among SnO<sub>2</sub> films thus far reported. Moreover, this value is close to the intrinsic limit of  $\mu_H$  calculated by assuming that only phonon and ionized impurities contribute to the carrier scattering.

## Results and Discussion

We first optimized the substrate temperature ( $T_s$ ) for growth of the TTO film, where the Ta content  $x$  was fixed at  $3 \times 10^{-3}$ . Figure 1(a) shows  $\omega$ - $2\theta$  X-ray diffraction (XRD) patterns for the TTO films prepared at various  $T_s$ . Only 002 diffraction peaks from SnO<sub>2</sub> and TiO<sub>2</sub> were observed in all the films, which indicated epitaxial growth of (001)-oriented SnO<sub>2</sub> films on TiO<sub>2</sub> (001) without any impurity phases. Epitaxial growth of the SnO<sub>2</sub> films were further confirmed by off-specular  $\Phi$ -scan of 101 diffraction peaks from SnO<sub>2</sub> and TiO<sub>2</sub> substrates (see Supplementary Fig. S1 online). Figure 1(b) shows the reciprocal space map observed around the asymmetric 112 diffraction peak for the TTO film grown at  $T_s = 600^\circ\text{C}$ . The film was almost fully relaxed, as reported<sup>16</sup> for undoped SnO<sub>2</sub> films on TiO<sub>2</sub> (001). Figure 1(c) plots the full width at half maximum of the rocking curve (FWHM<sub>002 $\omega$</sub> ) as a function of  $T_s$ . Notably, FWHM<sub>002 $\omega$</sub>  monotonically decreased with an increase of  $T_s$  and reached  $0.07^\circ$  at the highest  $T_s = 700^\circ\text{C}$ . This FWHM<sub>002 $\omega$</sub>  value is much smaller than that reported for the SnO<sub>2</sub> film on a thick self-buffer layer<sup>12</sup>, that is,  $0.31^\circ$ , which indicated very high crystallinity of the present TTO film. A similar trend, that is, improved crystallinity at high  $T_s$ , was reported in the previous research on SnO<sub>2</sub> epitaxial films<sup>23,25,26</sup>. The TTO films grown at higher  $T_s$  tended to exhibit higher  $\mu_H$ , as shown in Fig. 1(c). However, a slight decrease in  $\mu_H$  was observed for the film grown at

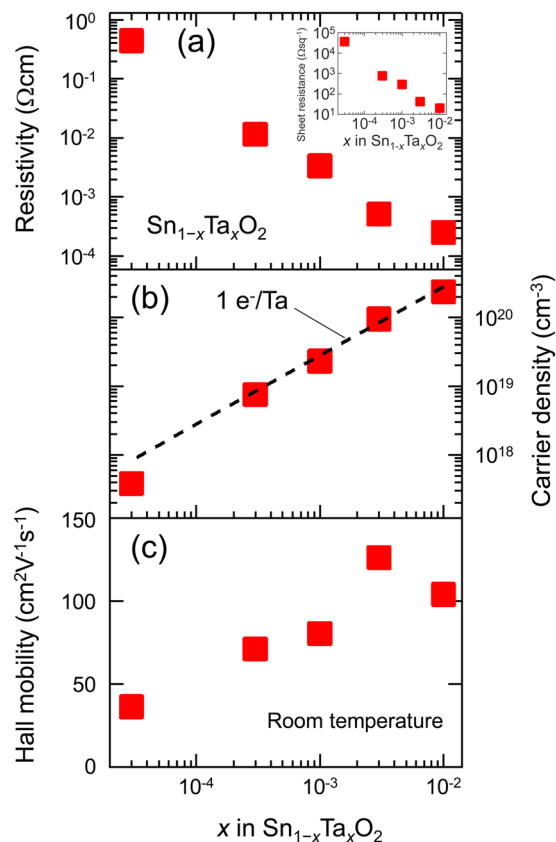


**Figure 2.** Room temperature (a) resistivity, (b) carrier density ( $n_e$ ), and (c)  $\mu_H$  for the TTO films as a function of  $x$ . The inset of (a) shows sheet resistance of the films. The broken line is the expected  $n_e$  when all the doped Ta<sup>5+</sup> ions substitute to the Sn<sup>4+</sup> sites and generate one electron per Ta (100% doping efficiency).

$T_s = 700$  °C in spite of the good crystallinity. We speculate that at such high  $T_s$ , interdiffusion of Sn and Ti atoms occurred at the film/substrate interface<sup>27</sup>, which might have caused impurity scattering and thus suppressed  $\mu_H$ . Hereafter we fixed  $T_s$  at 600 °C.

Next, we investigated the dependence of the transport properties of the TTO films on  $x$ . As shown in Fig. 2, the TTO film with the lowest  $x = 3 \times 10^{-5}$  showed  $n_e = 4 \times 10^{17}$  cm<sup>-3</sup> and  $\mu_H = 36$  cm<sup>2</sup>V<sup>-1</sup>s<sup>-1</sup>, which are close to those<sup>16</sup> reported for undoped SnO<sub>2</sub> films on TiO<sub>2</sub> (001). Furthermore,  $n_e$  was proportional to  $x$  and lay on the line representing a 100% doping efficiency, which indicated that each Ta<sup>5+</sup> ion generated one carrier electron. This implied that the lightly-doped TTO films were free from unfavourable defects such as clustered dopants<sup>28</sup> and acceptor-like defects<sup>29</sup>. Remarkably,  $\mu_H$  dramatically increased with increasing  $x$  at  $x \leq 3 \times 10^{-3}$ . This behavior was rationalized by assuming an enhanced screening of dislocations<sup>13</sup> and/or grain boundaries<sup>18,23</sup> owing to the increased  $n_e$ . The TTO films with  $x = 3 \times 10^{-3}$  ( $n_e \sim 1 \times 10^{20}$  cm<sup>-3</sup>) exhibited the highest  $\mu_H$  of 126–131 cm<sup>2</sup>V<sup>-1</sup>s<sup>-1</sup>, which is the highest among the  $\mu_H$  values reported for undoped and doped SnO<sub>2</sub> films so far. Further increase in  $x$  yielded a slight decrease in  $\mu_H$ , possibly owing to the manifestation of ionized impurity scattering, as will be discussed later. The lowest resistivity,  $2.5 \times 10^{-4}$  Ωcm, and sheet resistance, 20.2 Ωsq<sup>-1</sup>, were obtained for the TTO film with  $x = 1 \times 10^{-2}$ , as shown in Fig. 2(a).

We now discuss the transport properties of the TTO films in comparison with the literature data. Figure 3 plots  $\mu_H$  against  $n_e$  for thin films<sup>12,13,16,23</sup>, including ours, and bulk single crystals<sup>9,11</sup> of SnO<sub>2</sub>. The previously reported  $\mu_H$  values for thin films were generally lower than those of bulk single crystals with similar  $n_e$  values. However, our TTO films with  $n_e \sim 1 \times 10^{20}$  cm<sup>-3</sup> exhibited a record-high  $\mu_H$  (130 cm<sup>2</sup>V<sup>-1</sup>s<sup>-1</sup>) for thin films, which is comparable to that for a bulk single crystal with a similar  $n_e$  value. Such an extremely high  $\mu_H$  value suggests that the film contained a negligibly small amount of extrinsic sources of carrier scattering, such as neutral impurities, grain boundaries, and dislocations. In other words, intrinsic sources of carrier scattering, such as phonons and ionized impurities, supposedly dominated  $\mu_H$ .

To test the above-mentioned hypothesis, we calculated the Hall mobility ( $\mu_{cal}$ ) taking only phonon and ionized impurity scattering into account, as

$$\mu_{cal}^{-1} = \mu_{lat}^{-1} + \mu_{iis}^{-1},$$

where  $\mu_{lat}$  is the lattice mobility associated with phonon scattering and  $\mu_{iis}$  is the Hall mobility limited by ionized impurity scattering. For  $\mu_{lat}$  we used a fixed value (260 cm<sup>2</sup>V<sup>-1</sup>s<sup>-1</sup>) observed for undoped single crystals in the  $a$ -direction<sup>9</sup>. The  $\mu_{iis}$  value was calculated by using the Brooks–Herring–Dingle (BHD) formula<sup>30</sup>, which has

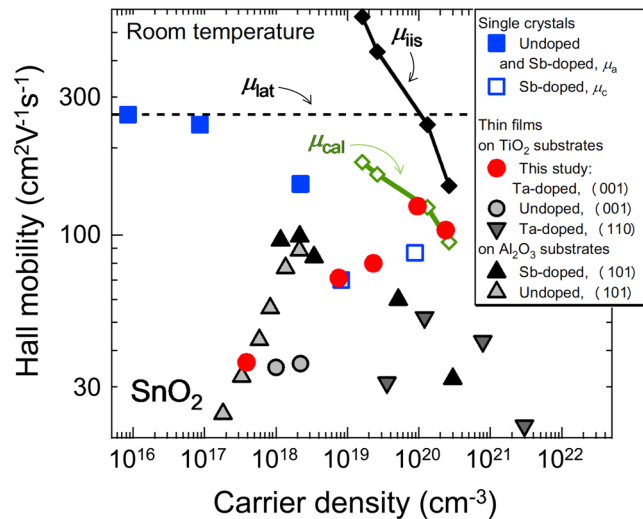


**Figure 3.** Room temperature  $\mu_H$  as a function of  $n_e$  for  $\text{SnO}_2$  bulk single crystals (squares) and thin films [circles (present study) and triangles (literature data)]. The data for undoped single crystals in the  $a$ -direction ( $\mu_a$ ) and Sb-doped single crystals in the  $c$ -direction ( $\mu_c$ ) are from refs. <sup>9,11</sup>, respectively. The data for Ta-doped (110)-, undoped (001)-, Sb-doped (101)-, and undoped (101)-films are from refs. <sup>23,16,12,13</sup>, respectively. A solid line with diamond symbols ( $\mu_{\text{cal}}$ ) represents calculated  $\mu_H$  assuming that only phonon ( $\mu_{\text{lat}}$ , broken line) and ionized impurity ( $\mu_{\text{iis}}$ , solid line) scattering contribute to  $\mu_H$  ( $\mu_{\text{cal}}^{-1} = \mu_{\text{lat}}^{-1} + \mu_{\text{iis}}^{-1}$ ).

been successfully used to analyze  $\mu_{\text{iis}}$  for Sn-doped  $\text{In}_2\text{O}_3$ <sup>31</sup>, Al-doped  $\text{ZnO}$ <sup>28,29</sup>, and Nb-doped  $\text{TiO}_2$ <sup>32</sup>. The BHD formula is written as

$$\mu_{\text{iis}} = \frac{24\pi^3(\epsilon_0\epsilon_r)^2\hbar^3n_e}{e^3m^{*2}F_{\text{ii}}Z^2n_1},$$

where  $\epsilon_0$  is the permittivity of free space,  $\epsilon_r$  is the relative static dielectric constant,  $\hbar$  is the reduced Planck's constant,  $e$  is the elementary charge, and  $m^*$  is the electron effective mass.  $Z$  and  $n_1$  are the charge and the density of the ionized impurity, respectively. The screening function  $F_{\text{ii}}$  is given by

$$F_{\text{ii}} = \ln(1 + 4/x) - (1 + x/4)^{-1}$$

with

$$\xi = \frac{e^2m^*}{\pi\epsilon_0\epsilon_r\hbar^2(3\pi^5)^{1/3}n_e^{1/3}}.$$

Considering the high doping efficiency, all the doped Ta was supposed to behave as singly charged ions ( $\text{Ta}^{5+}$  substituting for  $\text{Sn}^{4+}$ ). Although it was difficult to determine the valence state of Ta in TTO experimentally<sup>33</sup> (see Supplementary Fig. S3 online), theoretical calculations<sup>34,35</sup> reported that Ta exists in the pentavalent state ( $\text{Ta}^{5+}$ ) in TTO. Thus, we assumed  $Z = 1$  and  $n_1 = n_e$ . Because the films in this study were (001)-oriented, we used  $\epsilon_{\text{ra}} = 13.5$  for  $\epsilon_r$ <sup>36</sup>. For  $m^*$ , we used experimentally determined  $m_a^*$  values as a function of  $n_e$  and their linear interpolation<sup>37</sup>. As shown in Fig. 3,  $\mu_{\text{cal}}$  was higher than most of the experimental data, which indicated that the suppression of  $\mu_H$  arose from carrier scattering by extrinsic sources. Notably, however, the  $\mu_H$  values at  $n_e \geq 9 \times 10^{19} \text{ cm}^{-3}$  ( $x = 3 \times 10^{-3}$  and  $1 \times 10^{-2}$ ) in the present study agreed well with  $\mu_{\text{cal}}$ . This proved that in these high  $\mu_H$  films, carrier scattering by neutral impurities, dislocations, and grain-boundaries was negligibly small compared with that by ionized impurities and phonons, and that the reduced  $\mu_H$  at  $n_e = 2.4 \times 10^{20} \text{ cm}^{-3}$  ( $x = 1 \times 10^{-2}$ ) was attributed to the increased ionized impurity scattering.

To discuss the carrier scattering mechanisms in more detail, we measured temperature dependences of  $n_e$  and  $\mu_H$  for in the TTO films with  $x = 3 \times 10^{-4} - 1 \times 10^{-2}$ . As shown in Fig. 4(a), the  $n_e$  values were independent of temperature, indicating that the TTO films in this study were in the degenerately-doped regime. Notably, the TTO films with  $x \geq 1 \times 10^{-3}$  showed negative temperature coefficients of  $\mu_H$  (Fig. 4(b)) around room temperature, being the specific characteristic of phonon scattering. This implies that, at room temperature, the  $\mu_H$  values are dominated by phonon scattering, in consistence with the arguments based on the room temperature data (Fig. 3). At low temperature, phonon scattering is suppressed<sup>9</sup>, and ionized impurities are supposed to be the intrinsic sources of carrier scattering. Remarkably, as shown in Fig. 4(c),  $\mu_H$  at 10 K for the TTO film with  $x = 1 \times 10^{-2}$  ( $n_e = 2.4 \times 10^{20} \text{ cm}^{-3}$ ) agrees well with  $\mu_{\text{iis}}$ , which is known to be temperature-independent in degenerately-doped regime. This result supports the conclusion that  $\mu_H$  of the film is dominated by ionized impurity scattering and phonon scattering at room temperature (Fig. 3). As  $x$  and thus  $n_e$  decreased,  $\mu_H$  at 10 K started deviating downward from  $\mu_{\text{iis}}$ . This behaviour indicates that the TTO films with  $x < 1 \times 10^{-2}$  contain extrinsic

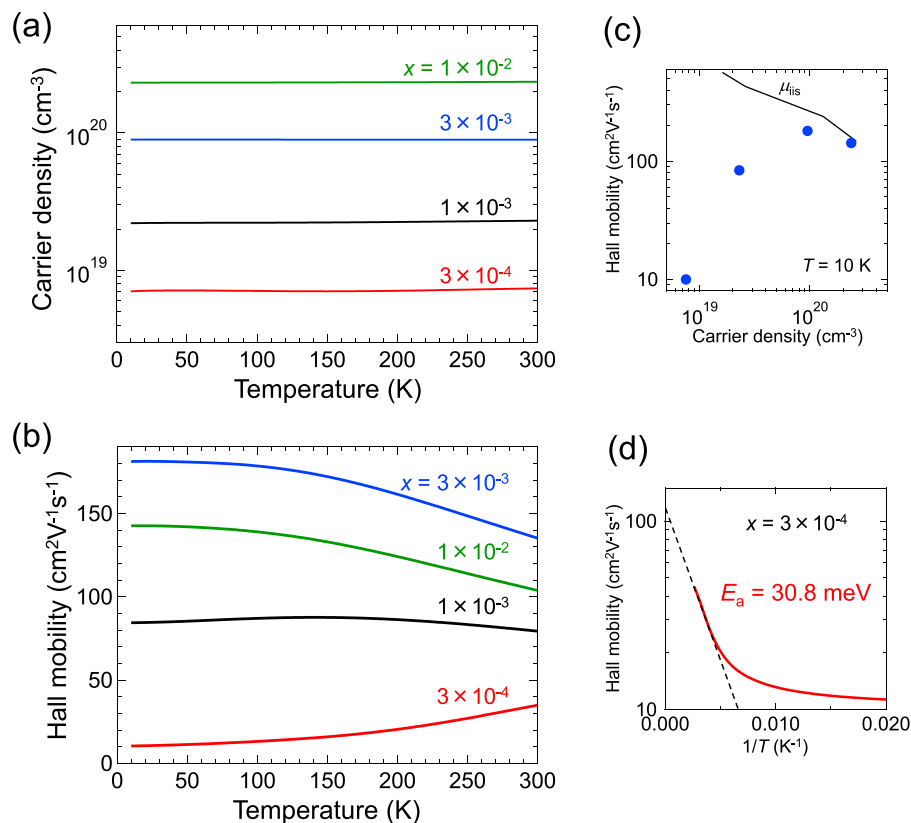


**Figure 4.** Temperature dependence of (a)  $n_e$  and (b)  $\mu_H$  for the TTO films with  $x = 3 \times 10^{-4} - 1 \times 10^{-2}$ . (c)  $\mu_H$  at 10 K (circles) as a function of  $n_e$ , in comparison with  $\mu_{iis}$  (solid line). (d)  $\mu_H$  for the TTO film with  $x = 3 \times 10^{-4}$  plotted against the inverse of temperature ( $1/T$ ). The dashed line represents the least-squares fit to the Arrhenius equation, yielding an activation energy value of 30.8 meV.

sources of carrier scattering, pronounced especially at low temperature. Thermal-activation-type behaviour of  $\mu_H$  was observed for the TTO film with  $x = 3 \times 10^{-4}$  (Fig. 4(d)), demonstrating that  $\mu_H$  is governed by grain boundary scattering<sup>38</sup> in the film, although grain-boundary scattering in SnO<sub>2</sub> epitaxial films has scarcely been studied so far. Dominguez *et al.* proposed that {101} crystallographic shear planes (CSPs) in SnO<sub>2</sub> films, which are induced by misfit dislocations<sup>39</sup>, may act like grain boundaries<sup>18</sup>. Similarly, we speculated that the carrier scattering at {101} CSPs was responsible for the lower  $\mu_H$  than  $\mu_{cal}$  at  $n_e < 9 \times 10^{19} \text{ cm}^{-3}$ .

Judging from the complete screening by free carriers at  $n_e \geq 9 \times 10^{19} \text{ cm}^{-3}$ , the CSP-based grain-boundary scattering in the TTO films was supposed to be weak. We considered that lattice matching and growth orientation play an essential role in the CSP-based grain-boundary scattering as follows. Owing to the good lattice-matching to SnO<sub>2</sub>, the TiO<sub>2</sub> (001) substrate would induce lower densities of misfit dislocations and thus CSPs in the films than other substrates<sup>18,39</sup>. Furthermore, the angle between {101} CSPs and the basal plane of the SnO<sub>2</sub> (001) film was approximately 34°, as shown in Fig. 5(a). The shallow angle would cause termination of the {101} CSPs at the crossing point with complementary {101} CSPs<sup>39</sup> at the early stage of the film growth. Indeed, as shown in Fig. 5(b), cross-sectional transmission electron microscopy (TEM) observations revealed that the TTO films on the TiO<sub>2</sub> substrate had lower densities of CSPs than those on other substrates<sup>18,39</sup> and that the CSPs did not reach the film surface, which supported the above-mentioned scenario. These structural characteristics can account for the lower contribution of carrier scattering at the CSP-based grain boundaries to the carrier transport in the TTO films on TiO<sub>2</sub> (001). However, SnO<sub>2</sub> epitaxial films on other substrates than TiO<sub>2</sub> (001) have reportedly shown highly populated {101} CSPs inclined steeply to the basal planes<sup>18,39</sup>, as schematically illustrated in Fig. 5(a). The CSPs in SnO<sub>2</sub> epitaxial films are induced by misfit dislocations, and they are not energetically favorable in bulk crystal, unlike the CSPs induced by off-stoichiometry, as seen in oxygen-deficient rutile TiO<sub>2</sub> crystals<sup>40</sup>. Therefore, the density of CSPs decreased as the film thickness increases<sup>18</sup>. Nevertheless, some of the CSPs in those films survived even near the surface of the films<sup>18</sup>. These results suggest that the CSP-based grain-boundary scattering is more significant in the SnO<sub>2</sub> epitaxial films on other substrates than TiO<sub>2</sub> (001), which can account for the lower  $\mu_H$  than those for the TTO films on TiO<sub>2</sub> (001), as depicted in Fig. 3.

To verify the proposed model, we investigated film thickness and growth orientation dependence of  $\mu_H$  for TTO films with  $x = 3 \times 10^{-3}$  grown on various substrates<sup>12-21,23-27,39,41,42</sup>, (001)-, (101)-, and (110)-planes of TiO<sub>2</sub>, and m-, r-, and c-planes of Al<sub>2</sub>O<sub>3</sub> substrates (see Supplementary Fig. S4 online). Figure 6 plots room temperature  $n_e$  and  $\mu_H$  for the TTO films with various film orientations as a function of the film thickness. With increasing film thickness, the  $\mu_H$  values increased probably owing to the synergistic effect of enlarged crystalline grains<sup>43,44</sup> and reduced density of threading dislocations<sup>24</sup> and {101} CSPs<sup>18,39</sup>. The highest  $\mu_H$  was achieved for the

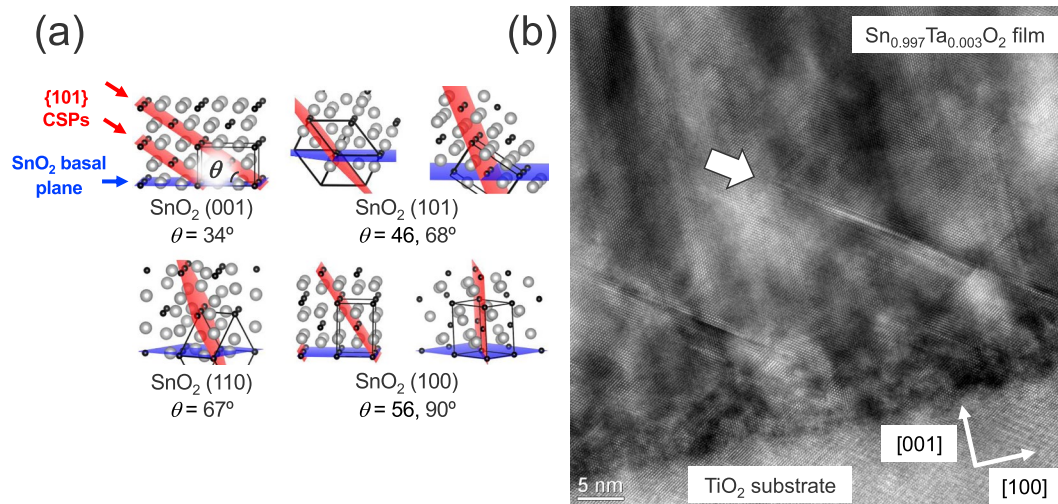


**Figure 5.** (a) Schematics of {101} planes, at which crystallographic shear planes (CSPs) are formed, against SnO<sub>2</sub> basal planes with (001), (101), (110), and (100) orientation using the VESTA program<sup>45</sup>.  $\theta$  denotes the angle between {101} and each SnO<sub>2</sub> basal plane. (b) Cross-sectional transmission electron microscopy image of a TTO film with  $x = 3 \times 10^{-3}$ . The incident electron beam was parallel to the [010] direction. The arrow in the film indicates {101} CSP.

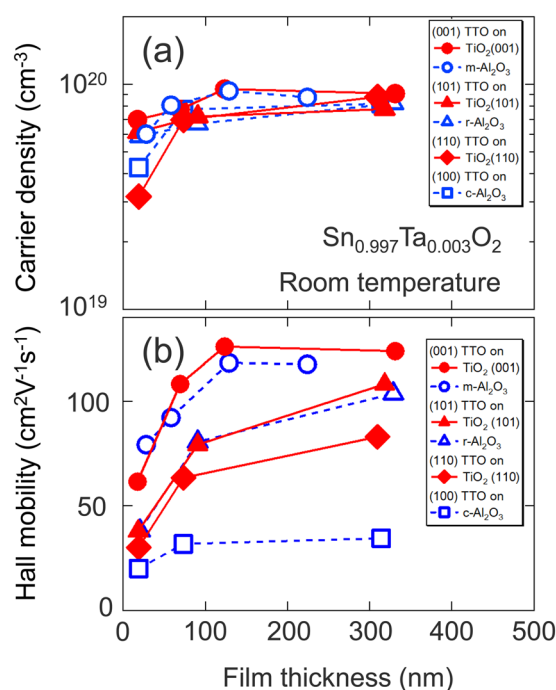


**Figure 6.** Film thickness dependence of room temperature (a)  $n_e$  and (b)  $\mu_H$  for the TTO films with (001) (circles), (101) (triangles), (110) (diamonds), and (100) (squares) orientations grown on TiO<sub>2</sub> (closed symbols) and Al<sub>2</sub>O<sub>3</sub> (open symbols) substrates.

(001)-oriented TTO films, followed in order by the (101)-, the (110)-, and the (100)-oriented ones. This behaviour can be explained by the CSP-based grain-boundary scattering because the angle between the CSP and the basal planes of the films becomes small in the same order (Fig. 5(a)). Notably, the TTO films with the same orientation showed similar  $\mu_H$  values even though different kinds of substrates were used. The orientation dependence of  $\mu_H$  cannot be explained by the anisotropy in electron effective mass of SnO<sub>2</sub> (see Supplementary Fig. S5 online). It was suggested that {101} CSPs play a significant role in the carrier transport in the TTO epitaxial thin films.

## Summary

We investigated the transport properties of  $\text{Sn}_{1-x}\text{Ta}_x\text{O}_2$  (TTO) films with  $x = 3 \times 10^{-5}$ – $1 \times 10^{-2}$  epitaxially grown on  $\text{TiO}_2$  (001) substrates. The  $n_e$  values for the TTO films were almost equal to the concentrations of Ta dopants, which demonstrated the very high doping efficiency of Ta. The  $\mu_{\text{H}}$  values of the TTO films with  $n_e \geq 9 \times 10^{19} \text{ cm}^{-3}$  ( $x \geq 3 \times 10^{-3}$ ) agreed well with the intrinsic limit of  $\mu_{\text{H}}$  assuming that only phonon and ionized impurities contributed to carrier scatterings. Negligible contribution of the grain-boundary scattering to  $\mu_{\text{H}}$  might arise from a reduced density of CSPs. The TTO films with  $n_e \sim 1 \times 10^{20} \text{ cm}^{-3}$  ( $x = 3 \times 10^{-3}$ ) exhibited a very high  $\mu_{\text{H}}$  of  $130 \text{ cm}^2 \text{ V}^{-1} \text{ s}^{-1}$ , which is the highest among  $\text{SnO}_2$  films thus far reported. The  $\mu_{\text{H}}$  values for the TTO ( $x < 3 \times 10^{-3}$ ) films rapidly decreased with a decrease of  $x$ , which suggested a weakened screening of dislocation and/or grain-boundary scatterings owing to the decreased  $n_e$ .

## Methods

TTO films with a thickness of 100–120 nm, with  $x = 3 \times 10^{-5}$ – $1 \times 10^{-2}$ , were grown on  $\text{TiO}_2$  (001) substrates by pulsed laser deposition (PLD) with a KrF excimer laser. TTO films with  $x = 3 \times 10^{-3}$  were grown (001)-, (101)-, and (110)-planes of  $\text{TiO}_2$ , and m-, r-, and c-planes of  $\text{Al}_2\text{O}_3$  substrates. The repetition rate and the fluence of the laser were set at 2 Hz and  $1\text{--}2 \text{ J} \cdot \text{cm}^{-2}$ , respectively. The typical growth rate was 0.14–0.17 Å per shot. Sintered pellets of TTO with  $x = 3 \times 10^{-4}$ – $1 \times 10^{-2}$  were used as PLD targets. TTO films with  $x = 3 \times 10^{-5}$  were fabricated by alternating ablation<sup>23</sup> of a commercial undoped  $\text{SnO}_2$  (4 N purity, Toshiba MFG) target and a TTO pellet with  $x = 3 \times 10^{-4}$ . In this study, nominal  $x$  values were used to represent the chemical compositions of the films because stoichiometric transfer of Ta from the targets to the films has been reported for TTO films grown under a similar condition<sup>23</sup>. The base pressure of the PLD chamber was maintained at  $3 \times 10^{-9}$  Torr. Oxygen partial pressure and  $T_s$  during film growth were  $1 \times 10^{-2}$  Torr and 400–700 °C, respectively. Crystal structure and crystallinity were evaluated by XRD measurements using a four-circle diffractometer (Bruker AXS, D8 DISCOVER). The cross-sectional microstructure of the films was observed by using a transmission electron microscope (FEI, Titan Cubed G2 60-300) operated at 300 kV. Hall effect and resistivity were measured by using a standard six-terminal method. The Hall-bar width and the distance between voltage terminals for four-probe measurements were 1 mm and 2.4 mm, respectively. Ag or In electrodes were used for ohmic contacts. A laboratory constructed system equipped with a 2 T electromagnet was used for room temperature measurements. Current–voltage characteristics and Hall voltage–magnetic field characteristics were measured repeatedly (at least twice) to confirm the reliability and reproducibility of the measurements. Temperature dependence of the transport properties was measured with a commercially available system (Quantum design, physical properties measurement system (PPMS Model 6000)).

## Data availability

The datasets during the current study are available from the corresponding author on reasonable request.

Received: 7 October 2019; Accepted: 1 April 2020;

Published online: 22 April 2020

## References

1. Yu, X., Marks, T. J. & Facchetti, A. Metal oxides for optoelectronic applications. *Nat. Mater.* **15**, 383–396 (2016).
2. Wei Shih, C., Chin, A., Fu Lu, C. & Fang Su, W. Remarkably high mobility ultra-thin-film metal-oxide transistor with strongly overlapped orbitals. *Sci. Rep.* **6**, 19023, <https://doi.org/10.1038/srep19023> (2016).
3. Das, S. & Jayaraman, V.  $\text{SnO}_2$ : A comprehensive review on structures and gas sensors. *Prog. Mater. Sci.* **66**, 112–255 (2014).
4. Vallejos, S. *et al.* Aerosol assisted chemical vapour deposition of gas sensitive  $\text{SnO}_2$  and Au-functionalised  $\text{SnO}_2$  nanorods via a non-catalysed vapour solid (VS) mechanism. *Sci. Rep.* **6**, 28464, <https://doi.org/10.1038/srep28464> (2016).
5. Palla Papavlu, A. *et al.* Highly sensitive  $\text{SnO}_2$  sensor via reactive laser-induced transfer. *Sci. Rep.* **6**, 25144, <https://doi.org/10.1038/srep25144> (2016).
6. Ellmer, K. Past achievements and future challenges in the development of optically transparent electrodes. *Nat. Photonics* **6**, 809–817 (2012).
7. Yang, J. K. *et al.* Reference of Temperature and Time during tempering process for non-stoichiometric FTO films. *Sci. Rep.* **5**, 15001, <https://doi.org/10.1038/srep15001> (2015).
8. Yu, S., Li, L., Lyu, X. & Zhang, W. Preparation and investigation of nano-thick FTO/Ag/FTO multilayer transparent electrodes with high figure of merit. *Sci. Rep.* **6**, 20399, <https://doi.org/10.1038/srep20399> (2016).
9. Fonstad, C. G. & Rediker, R. H. Electrical Properties of High-Quality Stannic Oxide Crystals. *J. Appl. Phys.* **42**, 2911 (1971).
10. Galazka, Z. *et al.* Growth, characterization, and properties of bulk  $\text{SnO}_2$  single crystals. *Phys. Status Solidi A* **211**, 66–73 (2014).
11. Morgan, D. F. & Wright, D. A. Electrical properties of single crystals of antimony-doped stannic oxide. *Br. J. Appl. Phys.* **17**, 337–340 (1966).
12. White, M. E., Bierwagen, O., Tsai, M. Y. & Speck, J. S. Electron transport properties of antimony doped  $\text{SnO}_2$  single crystalline thin films grown by plasma-assisted molecular beam epitaxy. *J. Appl. Phys.* **106**, 093704 (2009).
13. Mun, H., Yang, H., Park, J., Ju, C. & Char, K. High electron mobility in epitaxial  $\text{SnO}_{2-x}$  in semiconducting regime. *APL Mater.* **3**, 076107 (2015).
14. Semancik, S. & Cavicchi, R. E. The growth of thin, epitaxial  $\text{SnO}_2$  films for gas sensing applications. *Thin Solid Films* **206**, 81–87 (1991).
15. Rachut, K., Körber, C., Brötz, J. & Klein, A. Growth and surface properties of epitaxial  $\text{SnO}_2$ . *Phys. status solidi A* **211**, 1997–2004 (2014).
16. Okude, M. *et al.* Effect of *in situ* annealed  $\text{SnO}_2$  buffer layer on structural and electrical properties of (001)  $\text{SnO}_2/\text{TiO}_2$  heterostructures. *J. Phys. D* **41**, 125309 (2008).
17. Zhen, Y. *et al.* Investigations of growth kinetics of pulsed laser deposition of tin oxide films by isotope tracer technique. *J. Appl. Phys.* **108**, 1–7 (2010).
18. Dominguez, J. E., Fu, L. & Pan, X. Q. Effect of crystal defects on the electrical properties in epitaxial tin dioxide thin films. *Appl. Phys. Lett.* **81**, 5168–5170 (2002).
19. Kim, Y., Lee, S. W. & Chen, H. Microstructural evolution and electrical property of Ta-doped  $\text{SnO}_2$  films grown on  $\text{Al}_2\text{O}_3$  (0001) by metalorganic chemical vapor deposition. *Thin Solid Films* **405**, 256–262 (2002).

20. Feng, X. *et al.* Highly thermal stable transparent conducting SnO<sub>2</sub>:Sb epitaxial films prepared on  $\alpha$ -Al<sub>2</sub>O<sub>3</sub> (0001) by MOCVD. *Appl. Surf. Sci.* **254**, 6601–6604 (2008).
21. Luan, C., Zhu, Z., Mi, W. & Ma, J. Effect of Sb doping on structural, electrical and optical properties of epitaxial SnO<sub>2</sub> films grown on r-cut sapphire. *J. Alloys Compd.* **586**, 426–430 (2014).
22. Nakao, S. *et al.* High mobility exceeding 80 cm<sup>2</sup>V<sup>-1</sup>s<sup>-1</sup> in polycrystalline Ta-Doped SnO<sub>2</sub> thin films on glass using anatase TiO<sub>2</sub> seed layers. *Appl. Phys. Express* **3**, 031102 (2010).
23. Toyosaki, H., Kawasaki, M. & Tokura, Y. Electrical properties of Ta-doped SnO<sub>2</sub> thin films epitaxially grown on TiO<sub>2</sub> substrate. *Appl. Phys. Lett.* **93**, 132109 (2008).
24. Vashghani Farahani, S. K. *et al.* Influence of charged-dislocation density variations on carrier mobility in heteroepitaxial semiconductors: The case of SnO<sub>2</sub> on sapphire. *Phys. Rev. B* **86**, 245315 (2012).
25. Tsai, M. Y., White, M. E. & Speck, J. S. Plasma-assisted molecular beam epitaxy of SnO<sub>2</sub> on TiO<sub>2</sub>. *J. Cryst. Growth* **310**, 4256–4261 (2008).
26. White, M. E., Tsai, M. Y., Wu, F. & Speck, J. S. Plasma-assisted molecular beam epitaxy and characterization of SnO<sub>2</sub> (101) on r-plane sapphire. *J. Vac. Sci. Technol. A* **26**, 1300 (2008).
27. Palgrave, R. G., Bourlange, A., Payne, D. J., Foord, J. S. & Egdell, R. G. Interfacial diffusion during growth of SnO<sub>2</sub> (110) on TiO<sub>2</sub> (110) by Oxygen Plasma Assisted Molecular Beam Epitaxy. *Cryst. Growth Des.* **9**, 1793–1797 (2009).
28. Ellmer, K. Resistivity of polycrystalline zinc oxide films: current status and physical limit. *J. Phys. D* **34**, 3097–3108 (2001).
29. Jia, J., Oka, N., Kusayanagi, M., Nakatomi, S. & Shigesato, Y. Origin of carrier scattering in polycrystalline Al-doped ZnO films. *Appl. Phys. Express* **7**, 105802 (2014).
30. Dingle, R. B. Scattering of electrons and holes by charged donors and acceptors in semiconductors. *Philos. Mag.* **46**, 831–840 (1955).
31. Shigesato, Y. & Paine, D. C. Study of the effect of Sn doping on the electronic transport properties of thin film indium oxide. *Appl. Phys. Lett.* **62**, 1268–1270 (1993).
32. Furubayashi, Y. *et al.* Transport properties of d-electron-based transparent conducting oxide: Anatase Ti<sub>1-x</sub>Nb<sub>x</sub>O<sub>2</sub>. *J. Appl. Phys.* **101**, 093705 (2007).
33. Weidner, M., Brötz, J. & Klein, A. Sputter-deposited polycrystalline tantalum-doped SnO<sub>2</sub> layers. *Thin Solid Films* **555**, 173–178 (2014).
34. Behtash, M., Joo, P. H., Nazir, S. & Yang, K. Electronic structures and formation energies of pentavalent-ion-doped SnO<sub>2</sub>: First-principles hybrid functional calculations. *J. Appl. Phys.* **117**, 175101 (2015).
35. Williamson, B. *et al.* Resonant Ta Doping for Enhanced Mobility in Transparent Conducting SnO<sub>2</sub>. *Chem. Mater.* **32**, 1964–1973 (2020).
36. Summitt, R. Infrared absorption in single-crystal stannic oxide: Optical lattice-vibration modes. *J. Appl. Phys.* **39**, 3762–3767 (1968).
37. Feneberg, M. *et al.* Anisotropy of the electron effective mass in rutile SnO<sub>2</sub> determined by infrared ellipsometry. *Phys. Status Solidi A* **211**, 82–86 (2014).
38. Bruneaux, J., Cachet, H., Froment, M. & Messad, A. Correlation between structural and electrical properties of sprayed tin oxide films with and without fluorine doping. *Thin Solid Films* **197**, 129–142 (1991).
39. Wakabayashi, H., Suzuki, T., Iwazaki, Y. & Fujimoto, M. Defect Structure of Heteroepitaxial SnO<sub>2</sub> Thin Films Grown on TiO<sub>2</sub> Substrates. *Jpn. J. Appl. Phys.* **40**, 6081–6087 (2001).
40. Bursill, L. A. & Hyde, B. G. Crystallographic shear in the higher titanium oxides: structure, texture, mechanisms and thermodynamics. *Prog. Solid State Chem.* **7**, 177–253 (1972).
41. Kim, D. H., Kim, W.-S., Lee, S. B. & Hong, S.-H. Gas sensing properties in epitaxial SnO<sub>2</sub> films grown on TiO<sub>2</sub> single crystals with various orientations. *Sensors Actuators B Chem.* **147**, 653–659 (2010).
42. Kim, D. H., Kwon, J.-H., Kim, M. & Hong, S.-H. Structural characteristics of epitaxial SnO<sub>2</sub> films deposited on a- and m-cut sapphire by ALD. *J. Cryst. Growth* **322**, 33–37 (2011).
43. Agashe, C., Hüpkes, J., Schöpe, G. & Berginski, M. Physical properties of highly oriented spray-deposited fluorine-doped tin dioxide films as transparent conductor. *Sol. Energy Mater. Sol. Cells* **93**, 1256–1262 (2009).
44. Ishiki, M. *et al.* Improving Mobility of F-Doped SnO<sub>2</sub> Thin Films by Introducing Temperature Gradient during Low-Pressure Chemical Vapor Deposition. *Jpn. J. Appl. Phys.* **51**, 095801 (2012).
45. Momma, K. & Izumi, F. VESTA 3 for three-dimensional visualization of crystal, volumetric and morphology data. *J. Appl. Crystallogr.* **44**, 1272–1276 (2011).

## Acknowledgements

This work was supported by JSPS KAKENHI Grant Number 15K04687 and CREST, JST. S.N. gratefully acknowledges Ms. Reiko Nagashima of the University of Tokyo for her sincere encouragement. We thank Edanz Group ([www.edanzediting.com/ac](http://www.edanzediting.com/ac)) for editing a draft of this manuscript.

## Author contributions

S.N. conceived the project. M.F. grew and characterized the films with the help of S.N., K.S. and Y.H. D.O. and K.M. performed the TEM observations. T.H. supervised the project. M.F., S.N., Y.H. and T.H. wrote the manuscript with input from all authors.

## Competing interests

The authors declare no competing interests.

## Additional information

**Supplementary information** is available for this paper at <https://doi.org/10.1038/s41598-020-63800-3>.

**Correspondence** and requests for materials should be addressed to S.N.

**Reprints and permissions information** is available at [www.nature.com/reprints](http://www.nature.com/reprints).

**Publisher's note** Springer Nature remains neutral with regard to jurisdictional claims in published maps and institutional affiliations.



**Open Access** This article is licensed under a Creative Commons Attribution 4.0 International License, which permits use, sharing, adaptation, distribution and reproduction in any medium or format, as long as you give appropriate credit to the original author(s) and the source, provide a link to the Creative Commons license, and indicate if changes were made. The images or other third party material in this article are included in the article's Creative Commons license, unless indicated otherwise in a credit line to the material. If material is not included in the article's Creative Commons license and your intended use is not permitted by statutory regulation or exceeds the permitted use, you will need to obtain permission directly from the copyright holder. To view a copy of this license, visit <http://creativecommons.org/licenses/by/4.0/>.

© The Author(s) 2020